Experiments in Fluids (2023) 64:140
https://doi.org/10.1007/s00348-023-03677-w

RESEARCH ARTICLE

Bubble migration in containers with interior corners under microgravity conditions

Joshua McCraney[1] · Joshua Bostwick[2] · Mark Weislogel[3] · Paul Steen[1]

Received: 24 September 2022 / Revised: 15 May 2023 / Accepted: 3 July 2023
© The Author(s), under exclusive licence to Springer-Verlag GmbH Germany, part of Springer Nature 2023

Abstract

This study provides a post-flight analysis of video-recorded centimetric-scale bubble migration experiments performed aboard the International Space Station as part of the second Capillary Flow Experiments circa 2010 - 2016, currently archived to the NASA database available for download at https://psi.nasa.gov/. During the microgravity tests, air is displaced by perfectly wetting liquids within containers of varying geometry that include at least one interior corner. The displacements are driven by capillary pressure gradients along the interior corners resulting from the tapering container geometries pursued herein: linear, stepped, and vane tapers. The 12-year old archived video data is newly mined and digitized to collect dynamic bubble position data within the containers. From an interior corner flow perspective, time-dependent advancing and receding bubble front locations are quantified and compared to theoretical lubrication model predictions. We show that despite increased container complexity, the models adequately predict flow transients for the geometric families of container types tested and for the flow regimes achieved. Such flows serve as critical unit operations for passive no-moving-parts solutions for gravity-free fluid phase/bubble separations aboard spacecraft.

Extended author information available on the last page of the article

Published online: 27 July 2023

Graphical abstract

1 Introduction

Phase separations readily occur via buoyancy under terrestrial conditions, where, for example, heavier liquids fall while lighter gases rise. In nearly weightless 'microgravity' environments there is no notion of 'up' and 'down' since there is no gravity. Instead, surface tension, liquid properties, and surface geometries, herein referred to as capillarity, dictate the positioning of gas-liquid interfaces. Capillarity can be exploited to induce or retard spontaneous liquid migrations (Kubochkin and Gambaryan-Roisman 2022). Here container geometries dictate the rates of phase separation, with applications in bubble trapping (Bico and Quéré 2002), drainage (Weislogel and McCraney 2019; McCraney et al. 2021), bubble arrest (Lamstaes and Eggers 2017; Li et al. 2019), free surface morphology (Kolliopoulos et al. 2021), CO_2 scrubbing (Moher et al. 2019), among others. The prevalence and passivity of interior corners among spacecraft are readily exploited by fluid management devices to induce liquid migration along desired paths (Jaekle 1991; Chato and Martin 2006). While ubiquitous in microgravity environments, recent developments in terrestrial microsystems also exploit capillary phase separation, such as for thermodynamic and kinetic characterization of protein liquid-liquid phase separation (Stender et al. 2021). Recent microgravity passive phase separation analyses investigate rapid transients, the time scales of which are well suited for drop tower (Torres and Weislogel 2021) or parabolic flight (Bisht and Dreyer 2020) experiments. However, bubble migration occurs at time-scales larger than drop tower or parabolic flight conditions allow. Due to the expense of conducting large time scale experiments in microgravity, data are lacking, which limits theoretical predictions and numerical benchmarks. This work aims to fill this gap by providing large length and time scale experimental microgravity data for passive phase separations. We compare the experimental data to a lubrication model, and remark on model agreement, identifying the limitations thereof.

Bubbles within terrestrial microfluidic devices can be harmful to proper system function. This situation has led to the development of numerous bubble mitigation methods and devices (Peng et al. 2022). Provided the bubbles are small, when the Bond number condition $Bo \equiv \rho g r^2/\sigma \ll 1$, where ρ is the density difference across the liquid surface, g is the local acceleration field strength (i.e., gravity), r is the characteristic free surface length (i.e., bubble radius), and σ is the surface tension, the bubbles are essentially spherical. Such bubbles are relatively stiff and can lodge in undesirable locations, where they can merge, become wall-bound, and disrupt, if not obstruct, the liquid flow. Provided characteristic channel dimensions (i.e., diameters) are larger than the bubble diameter, buoyancy drives bubbles to the top walls of channels such that they do not fully occlude the passageway. Depending on the channel geometry and wetting conditions of the liquid, larger bubbles can fully occlude the passageways (Manning et al. 2011). The phenomena is highly exaggerated in reduced-gravity environments where $Bo \ll 1$ not because the bubble radii are microscale, but because the acceleration field is. Thus, bubbles in the microgravity environments aboard spacecraft suffer similar challenges as do microfluidic devices on earth. One outstanding example is the primary hydrolysis oxygen generator aboard the International Space Station (ISS) which has failed on numerous occasions due to a single bubble lodged in a circular inlet tube preventing the flow of water to the device (Korneva et al. 2005). A non-occluding conduit or other passive bubble mitigation method could solve the problem. However, at the 1000-fold larger length scales of 'capillary fluidic' systems aboard spacecraft, capillary flow rates, perturbations, and inertia are also increased to unearthly degrees requiring some minimal number of benchmark-level fluids experiments performed in space.

In part to this end, the Capillary Flow Experiments (CFE/CFE-2) were conducted aboard the ISS by NASA as a series of handheld, centimetric-scale liquid experiments designed to probe capillary phenomena of fundamental and applied importance including contact line dynamics (CFE-CL, Contact Line), critical wetting in discontinuous structures (CFE-VG, Vane Gap), and passive bubble migration and bubble separations (CFE-ICF, Interior Corner Flow) (Weislogel et al. 2004, 2009). Following completion of the experiments in flight, a NASA CFE video archive was made publicly available at https://psi.nasa.gov/. The data may be used to benchmark theoretical and numerical models for a variety of applications. The spaceflight data we analyse herein is mined from this resource.

Each CFE space experiment required the partial filling of a certain container with a perfectly wetting liquid, observing the response of the liquid for particular tests, and then draining that same liquid from the container. Approximately 2 to 3 hours of crew time were required for each operation which included time to retrieve, set-up, operate, and stow the hardware. Many dozens of operations were conducted between 2004 and 2017 on an 'as-crew-time-allows' basis (ISS task listed). Some 55 operations were conducted for the CFE-ICF containers alone (CFE and CFE-2). In this paper we are interested in air bubble migration in containers with interior corners–a passive means of bubble phase separation. We thus focus on the CFE-ICF experiments (CFE-2/ICF, completed between 2010 and 2016). Of the nine ICF test cell geometries sketched in Fig. 1, and of the many hundreds of individual test points recorded, only eight individual tests are analysed and reported herein. The results provide benchmarks for analytical and numerical methods predicting passive bubble migration within incrementally complex containers in low-g environments.

2 Experiment

The experiments we specifically analyze from the CFE-2 database were conducted over a 5-year period between 2010 and 2015. Figure 2 provides an annotated schematic, solid model, and wire model sketch for the ICF-9 vessel–a tapered isosceles triangle-based pyramid (cf. Fig. 1, ICF-9). For a partially filled vessel, the taper of the container provides a passive means of bubble migration and separation (Weislogel et al. 2011). We briefly describe the ICF bubble migration experiment protocol. The ICF vessel was placed on an ISS workbench, back-lit by a diffuse light screen via cabin and portable lighting, and filmed via an HD Canon XF305 video camcorder at 30 to 60 fps. The Test Chamber was partially-filled with prescribed liquid volume, where the astronaut then opened Valve 1 or 2 of the primary acute interior corner of the vessel and positioned the bubble at the small container end. The particular valve was then closed and the air bubble migrated passively through the Test Chamber. An annotated sketch of the flow is provided in Fig. 3 with profile and sectional views. Figure 4 provides time-stamped side perspectives of a bubble event for ICF-1 and ICF-3. Since the liquid wets the container walls it flows to the small end, thereby forcing the air bubble to the large end. This corner flow is driven by the capillary pressure gradient created by the differing fluid heights. The container geometry, fluid properties, and initial fill volume serve as the independent variables of the tests. Here we investigate Test Chambers with tapered cross-sections, stepped geometries, and complex vane networks.

The CFE-ICF video data on the NASA archive is digitally reduced and analyzed herein, yielding time-dependent interface profiles and bulk meniscus velocities. In reference to Fig. 3, the primary objective is to digitize the fluid interface for the advancing $z_2(t)$ and receding $z_1(t)$ bulk menisci and interior corner height profiles $h(z, t)$. We employ in-house developed automated interface tracking algorithms to digitize the data (Weislogel and McCraney 2019; McCraney et al. 2020). In brief, we first convert the video to low-loss

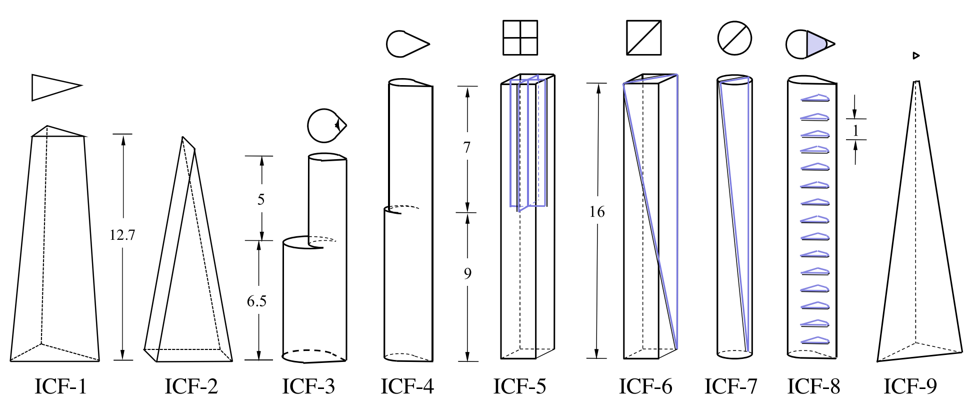

Fig. 1 Wire model sketches of ICF test cells with dimensions in cm

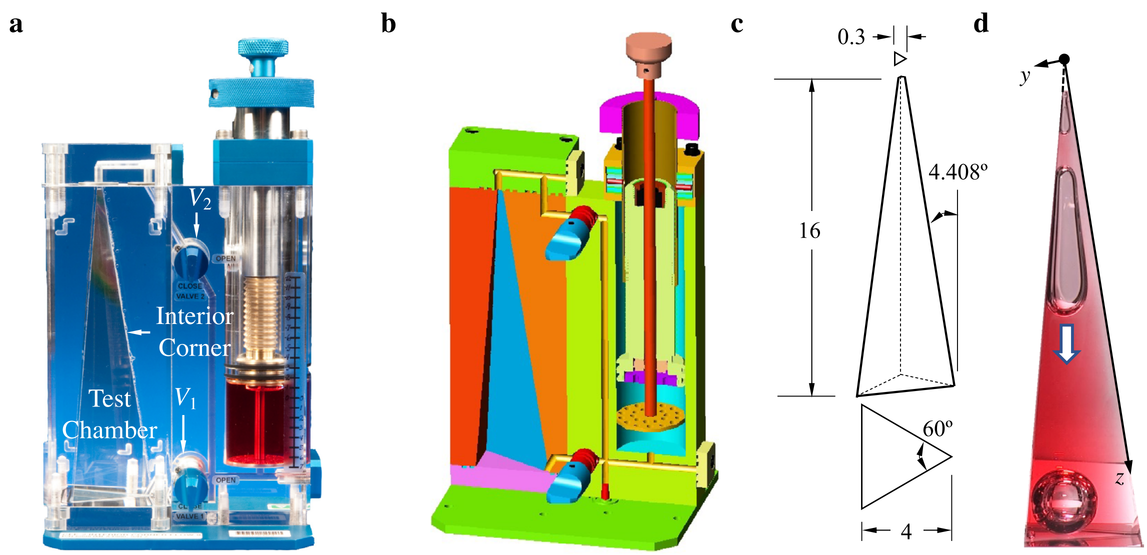

Fig. 2 Schematic of ICF-9 test vessel: a slender truncated equilateral triangle-based pyramid with 4.408° tapering faces. **a** Camera view of apparatus with valves V_1 and V_2 identified, **b** solid model, **c** tapered Test Chamber wire model with dimensions in cm and **d** cropped and overlaid initial and final images of Test Chamber bubble test with coordinate origin and blue arrow indicating the direction of bubble migration

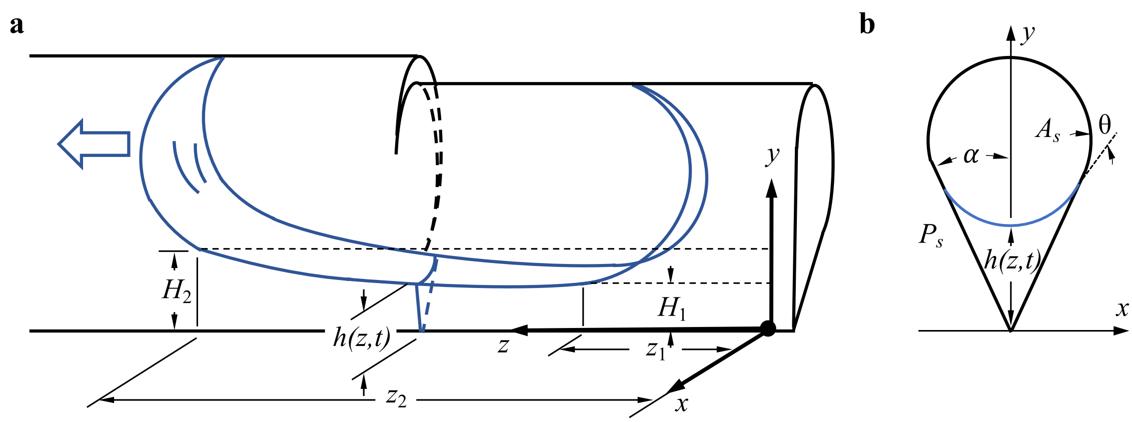

Fig. 3 Sketch of bubble migration for vessel ICF-4 in **a** perspective profile and **b** cross-sectional view. Arrow denotes direction of bubble migration

still images and then binary files. To reduce image noise due in part to small sparse air bubbles and spurious reflections, we employ a Canny filter (Canny 1986) applying two thresholds for edge detection sensitivity. We then loop through the region of interest for each image and tabulate the desired interface pixels. This process is performed many hundreds of times totaling over 2.5 h of low-g bubble data over thousands of pixels for each still frame. The intermediate interface detection data are then passed through a moving-average filter establishing smoothed meniscus profiles. Further details of the data are provided in the Supplemental Material.

3 Lubrication model

A theoretical prediction of capillary drainage from 'tapering' containers with interior corners (Weislogel et al. 2011) exploits the lubrication approximation for slender flows. We summarize the key details of the theory herein to compare to the newly reduced experimental data. Figure 3a provides a sketch of the bubble problem for the ICF-4 container, where the z-axis runs along the interior corner vertex and defines the primary flow direction. For wetting liquids satisfying the Concus-Finn corner wetting condition (Concus and Finn 1969),

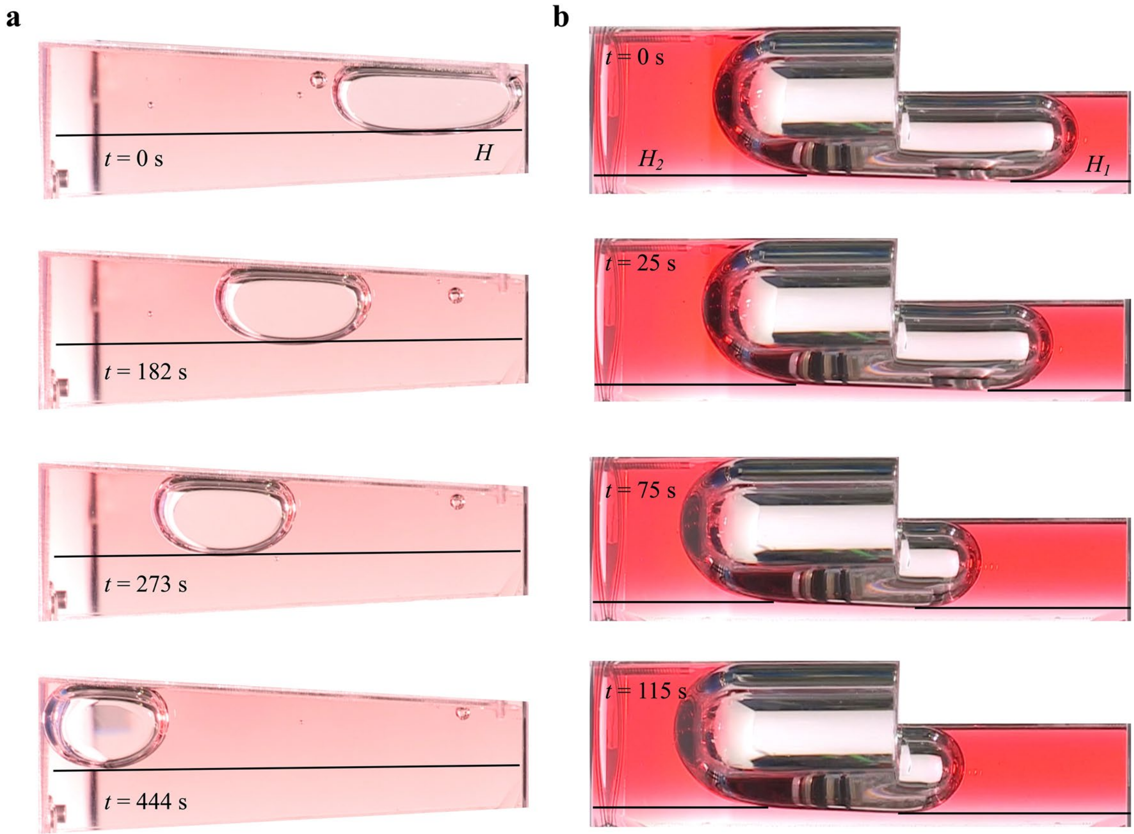

Fig. 4 Time-stamped images of bubble migration in the **a** tapered ICF-1 and **b** stepped ICF-3 test vessels with predicted height H (black line)

the bulk fluid interfaces establish quasi-steady equilibrium configurations, which feed capillary pressure/height conditions into the weakly varying elevation of the corner flows where the cross-sectional meniscus profiles are composed of nearly circular arcs as sketched in Fig. 3b. Since the flow is characterized by 1-d cross-flow curvature as depicted in Fig. 3b, the capillary pressure can be modelled as $P(z) = -\sigma(1/R_1 + 1/R_2) \approx -\sigma/R$ (low streamwise curvature implies $|R_2| \gg |R_1| \equiv R$), where $R = R(z,t) = fh(z,t)$ with cross-flow interface curvature function $f = \sin\alpha/(\cos\theta - \sin\alpha)$ (Weislogel et al. 2011), where α is the interior corner half-angle and θ is the liquid contact angle ($= 0°$ in this study). Thus, liquid at lower meniscus elevations achieves more negative pressures than at higher elevations, inducing a capillary pressure gradient that drives liquid from higher to lower elevations. As the incompressible liquid wicks toward the narrower end of the chamber, the bubble is forced toward the larger end as required by mass conservation. The more hemispherical 2-d curvature end cap regions are referred to as bulk flow regions. These are characterized by quasi-steady advancing ($z_2(t)$) and receding ($z_1(t)$) bulk menisci. The dynamical boundary condition $H_i(z_i;t)$ provides a matching region/condition between effectively 2-d bulk and 1-d corner flow regimes for the small H_1 and large H_2 elevations.

3.1 Stepped & tapered conduits

In general (Weislogel and Lichter 1998; Weislogel 2001), we assume slender container geometries with n geometrically wetted interior corners satisfying the Concus-Finn condition, where j serves as an index for the jth of n wetted corners; $j = 1, 2, ...n$. Figure 3 depicts the ICF-4 container with a single $n = 1$ interior corner of half-angle α_j. The flow is largely parallel to the contact line, permitting a constant contact angle θ condition. As demonstrated from a priori predictions (de Lazer et al. 1996; Finn and Neel 1999; Weislogel and Collicott 2004) and a posteriori measurements (Weislogel and Lichter 1998; McCraney et al. 2020; Weislogel 2001; Weislogel et al. 2007), it can be shown for quasi-steady liquids in semi-infinite columns under zero-gravity conditions that

$$H_j = \frac{P_s \cos\theta}{2\Sigma f_j}\left(1 - \left(1 - \frac{4\Sigma A_s}{P_s^2 \cos^2\theta}\right)^{1/2}\right), \tag{1}$$

where $P_s(z)$ and $A_s(z)$ are the container cross-sectional perimeter and area, respectively, which are functions of z (black lines in Fig. 4). Here Σ, F_{Aj}, and f_j are the dimensionless normalized total wetted corner cross-sectional flow area, jth corner cross-sectional flow area, and jth corner cross-flow interface curvature functions, respectively:

$$\Sigma = \sum_{j=1}^{n} \frac{F_{Aj}}{f_j^2}, \quad F_{Aj} = f_j^2\left(\frac{\cos\theta \sin\delta_j}{\sin\alpha_j} - \delta_j\right), \quad f_j = \frac{\sin\alpha_j}{\cos\theta - \sin\alpha_j}, \tag{2}$$

where $\delta_j \equiv \pi/2 - \alpha_j - \theta$. H_j serves as the key dynamical boundary condition for the corner flow analysis. Because H_j is known as a function solely of the geometry and wetting conditions of the container, it is known a priori and used to scale the governing momentum equations. Thus, by choosing scales

$$z \sim L, \quad h \sim H, \quad t \sim A_s L/Q_s, \quad Q_s \sim \sum_{j=1}^{n} F_{A\,j} F_{i\,j} H_j^3/L, \tag{3}$$

and assuming a slender interior corner flow satisfying $H_j^2/L^2 \ll 1$, the governing system reduces to a single dimensionless z-component visco-capillary momentum equation which may be solved along with the continuity equation to find solutions for the dimensionless height $h_j(z,t) = h_1(z,t) \equiv h(z,t)$, and advancing $z_2(t)$ and receding $z_1(t)$ bulk meniscus positions (Weislogel 1996; Weislogel and Lichter 1998; Weislogel et al. 2011). We note that $F_i = F_i(\alpha, \theta)$ is a weak geometric viscous flow resistance function (Weislogel 1996) such that $1/8 \leq F_i \leq 1/6$. The aforementioned analysis admits an analytic solution for bubble height for containers of types ICF-1,-3,-4,-5,-9:

$$h(z,t) = \left(z_2^3 + \frac{z_2^3 - z_1^3}{(z_2 - z_1)}(z - z_2)\right)^{1/3}. \tag{4}$$

When applied to stepped geometries (ICF-3,-4,-5), first-order asymptotic self-similar solutions for advancing and receding fronts are implicitly given by

$$z_1(t) = \frac{1 - \sqrt{1 - 2(1 - b^2 - b^3 + b^5)t/3}}{1 - b^2}, \tag{5}$$

$$z_2 = 1 + b^2 z_1. \tag{6}$$

where $b \equiv H_1/H_2$.

For tapered geometries, similar to previous works (Weislogel et al. 2007), it can be shown for quasi-static liquids in semi-infinite columns under microgravity conditions that

$$L = H_i\left(\frac{3V_u}{A_s}\right)^{1/3}, \tag{7}$$

where

$$V_u = \frac{z_2^3(0) - z_1^3(0)}{3}\left(A_s - F_{A\,i} H_i^2\right). \tag{8}$$

When applied to pyramidal tapered conduits (ICF-1,-9), first-order asymptotic self-similar solutions for advancing and receding fronts are implicitly given by

$$t = \frac{3}{4}\left((1 + z_1^3)^{4/3} - z_1^4 - 1\right) \tag{9}$$

$$z_2 = (1 + z_1^3)^{1/3}. \tag{10}$$

4 Results

We present the experimental results for various test cells and compare them to the lubrication predictions of advancing and receding bubble fronts $z_{1/2}$ and bubble height h. The theoretical predictions for both the stepped ICF-3,-4,-5 and tapered ICF-1,-9 compare favorably to experiment. ICF-2,-6,-7 are irregular tapers or contain a bisecting vane, the complexities of which are not easily reduced for experimental comparisons (ICF-2), or do not readily conform to the lubrication analysis. However, the processed data has been archived for future use. We note all experimental results analyzed exhibit tracking error within ±1 pixel, which implies tracked pixel location is within 0.2 mm for all experiments analyzed. Further details of the experimental data archival process can be found in the Supplemental Material.

4.1 Tapered conduits ICF-1,-9

Figure 5 plots bubble results for both tapered vessels ICF-1,-9. The ICF-1 experiments and theory show excellent agreement, as maximum error for both advancing and receding fronts for all runs is within ±5%, as shown in Fig. 5a. The self-similar meniscus height solution (4) also compares favorably to experiment, with average agreement within ±8%, as shown in Fig. 5c.

The ICF-9 test cell bubble advancing and receding fronts initially agree well with lubrication predictions, but as migration ensues deviations are observed, as shown in Fig. 5b. This result is expected in part due to the larger taper $\psi = 4.408°$ of ICF-9, where faster migration from

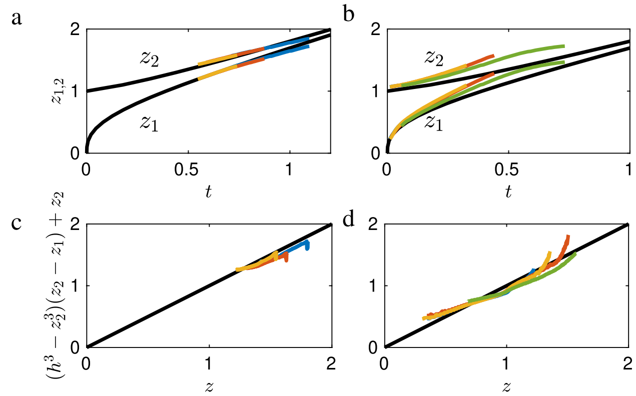

Fig. 5 Results from the tapered geometries of **(a, c)** ICF-1 and **(b, d)** ICF-9 test vessels presenting **(a, b)** advancing z_2 and receding z_1 bubble fronts and **(c, d)** self-similar bubble height $(h^3 - z_2^3)(z_2 - z_1) + z_2$ with axial coordinate z. Each color signifies a single bubble migration experiment which is compared to theory (black)

narrow to large ends is observed, as captured by the volumetric flow rate Q_s, and therefore the height dependence H_j, on $P_s(z)$ and $A_s(z)$, (2). Despite this reduction in fidelity to the lubrication model assumptions, both bubble fronts show maximum error within 16% when compared with experiment. The bubble height agrees well with experiment showing average error within ±9%, as presented via self-similar scales in Fig. 5d.

4.2 Stepped conduits ICF-3,-4,-5

Bubble transients are presented in Fig. 6 for stepped vessels ICF-3,-4,-5. The bubble advancing and receding fronts z_2 and z_1 (color) qualitatively agree with theoretical predictions (black), as shown in Fig. 6a-c. Average agreement for both fronts across all runs for ICF-3,-4,-5 is within 20%, 23%, and 23%, respectively. The lubrication solution predicts the meniscus height temporal evolution remarkably well, as shown in Fig. 5d-f. Average height agreement for vessels ICF-3,-4,-5 are within 13%, 16%, and 5%, respectively. Here we expect good agreement for the ICF-3,-4 geometries, as these conduits conform well to the model assumptions. It is interesting, however, that despite the lubrication prediction neglecting inertia, the model accurately predicts these non-negligible inertial flows, Table 2. Additionally, the simple lubrication model does well to predict the somewhat confounded stepped geometry created by the vane-network of ICF-5. Despite the geometric complications, the model accurately predicts bubble displacement, giving confidence to the utilization of the theory as a design guide for applications (Table 1).

4.3 Irregular conduits ICF-2,-6,-7

Bubble migration experiments were also analyzed in the irregular tapered cell of ICF-2, Fig. 1. Since the taper does not conform to the pyramidal taper of ICF-1,9, the lubrication theory is not applicable to this flow. However, the bubble migration data (advancing/receding fronts) for ICF-2, while not presented here, are available for download at McCraney (2023). We note the interfacial height is not available for this test cell, as both the viewing perspective of the camera and the interior corners are orthogonal to the side wall and not the corner flow interface profile.

Also analyzed are bubble migration experiments in the tapered-vane cells ICF-6,-7 which are constant cross section conduits shown in Fig. 1. The tapered vane establishes a capillary pressure gradient ($H_2 > H_1$) driving the liquid (bubble) toward (away from) the diagonally divide end. Figure 7 presents timestamped images of such passive bubble migration flows in the ICF-7 test cell, with measured interfacial height shown for reference. For these geometries, no current lubrication prediction exists for data comparison, so we omit further results, but note that multiple bubble tests for these vessels have been analyzed and are available for download at McCraney (2023). Measured quantities include dimensional bubble advancing/receding front locations as functions of time and bubble interfacial height, as plotted in Fig. 7b. For this specific test vessel, a vane accounting for 3% of the total tank volume passively repositions liquid and gas in minutes, offering passive fluid control with small cost in conduit/tank volume.

5 Conclusion

We reduce the data of spaceflight experiments of passive bubble migration flows in a number of conduits/vessels with interior corners from the Capillary Flow Experiment performed aboard the ISS. The flow conditions and conduits analyzed are such that the lubrication approximation can be applied to the flow, which admits analytic solutions for the bubble shape as a function of time. Comparing these analytical solutions with the experimental shows favorable agreement, which builds confidence in the model and modeling assumptions. The experimental data is detailed in the Supplemental Material made publicly available as simple MATLAB files (McCraney 2023), providing practical benchmarks for further model development and the verification and validation of numerical methods. The lubrication model solutions validated herein allow one to optimize container shapes for specific applications. In space, the results can be used to design specific capillary fluid elements for

Table 1 ICF-1,-9 fluid properties, average scales, and average constraints for all runs. Subscript 1 denotes the primary α_1 corner

Property	Units	ICF-1	ICF-9
Density, ρ	kg m^{-3}	950	950
Viscosity, μ	kg m^{-1} s^{-1}	0.019	0.019
Surface tension, σ	N m^{-1}	0.0206	0.0206
Contact angle, θ	deg	0°	0°
Scales	Units	ICF-1	ICF-9
Half angle, α_1	deg	15°	30°
Flow length, $L = \left(3V_u/F_{AS}\right)^{1/3}$	mm	216	77
Height, $H_1 = LF_R/f_1$	mm	11.6	6.5
Perimeter, P_s	mm	66	85
Surface area, A_s	mm^2	1100	346
Geometry, $F_{i\,1}$	–	0.141	0.129
Velocity, $W_1 = \sigma \sin^2 \alpha_1 F_{i\,1}/\mu f_1$	mm s^{-1}	1.6	2.9
Flow rate, $Q = \sum_j W_j F_{A\,j} H_j^3/L$	mm^3 s^{-1}	1348	1433
Time, $t \sim A_s L/Q$	s	982	460
Time offset, t_0	–	0.5544	0.0579
Lubrication assumptions	Constraint	ICF-1	ICF-9
Slender geometry, $\epsilon_1 = H_1/L$	$\epsilon_1^2 \ll 1$	10^{-3}	10^{-3}
Capillary dominance	$Bo \ll 1$	10^{-4}	10^{-4}
Low streamwise curvature	$\epsilon_1^2 f_1 \ll 1$	10^{-3}	10^{-3}
Low inertia	$\epsilon_1^2 \rho\sigma H_1 \sin^4 \alpha_1/(f_1 \mu^2) \ll 1$	10^{-2}	10^{-1}
Low normal stress	$\epsilon_1^2 \sin^2 \alpha_1 \ll 1$	10^{-4}	10^{-3}
Low saturation limit	$\beta/(1-\beta) \ll 1$	10^{-9}	10^{-9}
Static CL	$\epsilon_1 \beta \sin^2 \alpha_1/f_1 \ll 1$	10^{-11}	10^{-10}
Concus–Finn wetting	$\theta < 90° - \alpha_1$	Satisfied	Satisfied

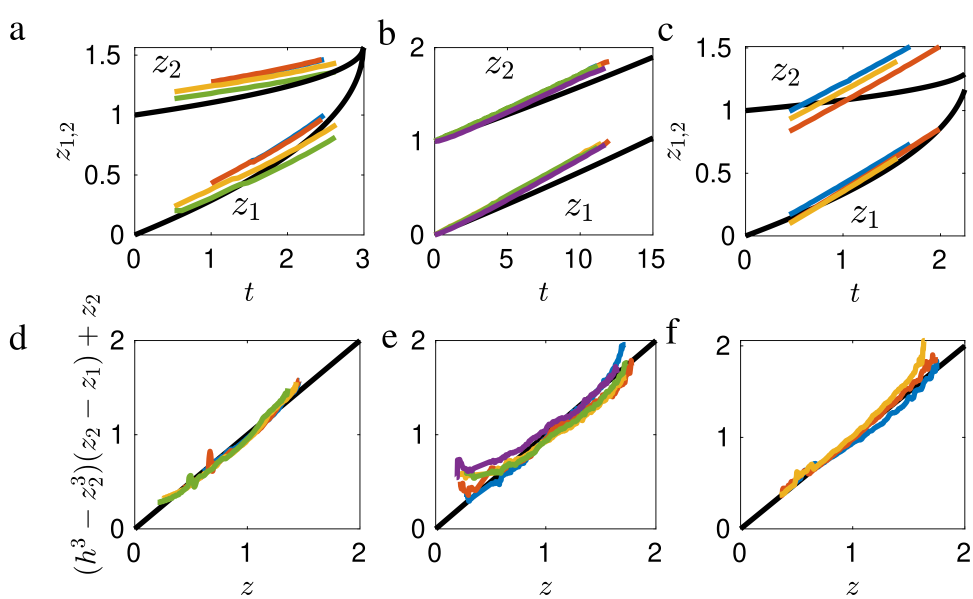

Fig. 6 Results from stepped vessel geometries **(a, d)** ICF-3, **(b,e)** ICF-4, and **(c, f)** ICF-5 plotting **(a, b, c)** advancing z_2 and receding z_1 bubble fronts and **(d, e, f)** self-similar meniscus height $(h^3 - z_2^3)(z_2 - z_1) + z_2$ against axial coordinate z. Each color signifies a single bubble migration experiment, which is compared to theory (black)

large length scale passive capillary fluidic control for flues, coolants, and water processing equipment for life support. On earth, the results may be employed for passive bubble management in microfluidic systems.

Table 2 ICF-3,-4,-5 fluid properties, average scales, and average constraints for all runs. Subscript 1 denotes the primary α_1 corner

Property	Units	ICF-3	ICF-4	ICF-5
Density, ρ	kg m^{-3}	839	839	839
Viscosity, μ	kg m^{-1} s^{-1}	0.0017	0.0017	0.0017
Surface tension, σ	N m^{-1}	0.0180	0.0180	0.0180
Contact angle, θ	deg	0°	0°	0°
Scales	Units	ICF-3	ICF-4	ICF-5
Half angle, α	deg	45°	25°	45°
Flow length, L	mm	60	55	80
Height, H	mm	3.2	7.3	2.2
Perimeter, P_s	mm	107	83	80
Surface area, A_s	mm^2	803	418	400
Geometry, F_i	–	1/7	0.133	1/7
Velocity, $W = \sigma \sin^2 \alpha F_i / \mu f$	mm s^{-1}	313	344	313
Flow rate, $Q \sim W F_A H^3 / L$	mm^3 s^{-1}	204	1062	26
Time, $t \sim A_s L / Q$	s	235	18	308
Time offset, t_0	–	0.5	0	0.45
Lubrication assumptions	Constraint	ICF-3	ICF-4	ICF-5
Slender geometry, $\epsilon = H/L$	$\epsilon^2 \ll 1$	10^{-3}	10^{-2}	10^{-4}
Capillary dominance	$Bo \ll 1$	10^{-4}	10^{-4}	10^{-4}
Low streamwise curvature	$\epsilon^2 f \ll 1$	10^{-3}	10^{-2}	10^{-3}
Low inertia	$\epsilon^2 \rho \sigma H \sin^4 \alpha / (f \mu^2) \ll 1$	4	29	10^{-1}
Low normal stress	$\epsilon^2 \sin^2 \alpha \ll 1$	10^{-3}	10^{-3}	10^{-4}
Low saturation limit	$\beta/(1-\beta) \ll 1$	10^{-2}	10^{-2}	10^{-2}
Static CL	$\epsilon \beta \sin^2 \alpha / f \ll 1$	10^{-4}	10^{-3}	10^{-5}
Concus-Finn wetting	$\theta < 90° - \alpha$	Satisfied	Satisfied	Satisfied

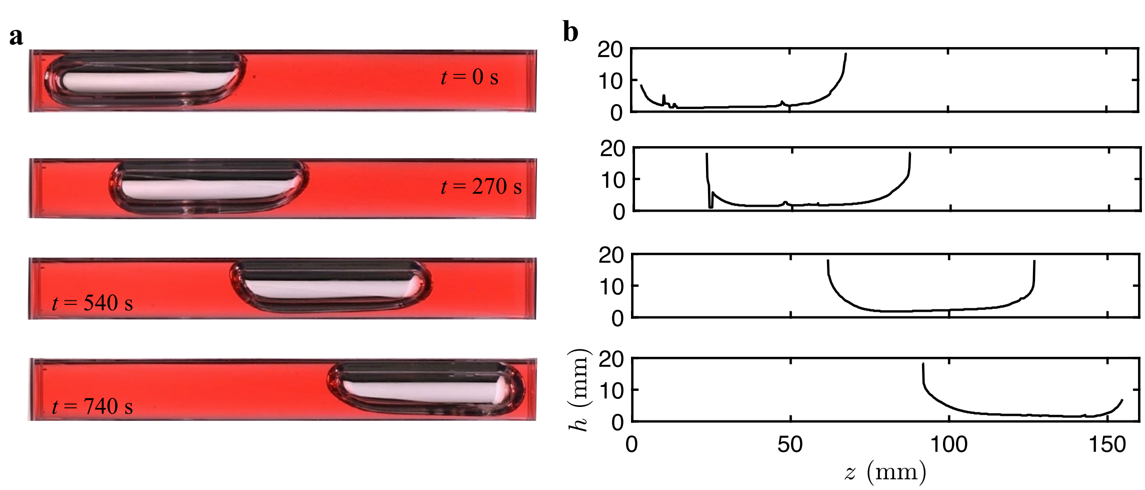

Fig. 7 ICF-7 experiment in **a** side view during bubble migration with and **b** corresponding bubble height data as detected from the image tracking algorithm

Supplementary Information The online version contains supplementary material available at https://doi.org/10.1007/s00348-023-03677-w.

Acknowledgements The authors thank the ISS astronaut crews–in this case NASA astronauts Scott Kelly, Cady Coleman, Michael Hopkins, Kevin Ford, Karen Nyberg and JAXA astronaut Koichi Wakata. We dedicate this work to Paul Steen (1952 - 2020).

Author Contributions JM wrote the manuscript and analyzed the experiments and compared the results to theory. JB and MW edited and assisted writing. PS guided the research.

Funding This work was supported in large part through NASA Grant 80NSSC19K0406 and NSF Award 1637960. M.W. is supported in part though NASA Cooperative Agreement 80NSSC18K0436.

Data availability All data will be uploaded to a public database upon publication decision, the location of which will appear here.

Declarations

Conflict of interest The authors declare no competing interests.

Ethical approval Not applicable.

References

Bico J, Quéré D (2002) Rise of liquids and bubbles in angular capillary tubes. J Colloid Interface Sci 247(1):162–166

Bisht KS, Dreyer ME (2020) Phase separation in porous media integrated capillary channels. Micrograv Sci Technol 32(6):1001–1018

Canny J (1986) A computational approach to edge detection. IEEE Trans Pattern Anal Mach Intell PAMI8(6):679–698. https://doi.org/10.1109/TPAMI.1986.4767851

Chato DJ, Martin TA (2006) Vented tank resupply experiment: flight test results. J Spacecr Rockets 43(5):1124–1130

Concus P, Finn R (1969) On the behavior of a capillary surface in a wedge. Proc Natl Acad Sci 63(2):292–299. https://doi.org/10.1073/pnas.63.2.292

de Lazer A, Langbien D, Dreyer M, Rath HJ (1996) Mean curvature of liquid surfaces in cylindrical containers of arbitrary cross-section. Micrograv Sci Technol 9(3):208–219

Finn R, Neel RW (1999) C-singular solutions of the capillary problem. J Reine Angew Math 512:1–25

Jaekle DE (1991) Propellant management device conceptual design and analysis-vanes. In: 27th Joint Propulsion Conference, page 2172

Kolliopoulos P, Jochem KS, Johnson D, Suszynski WJ, Francis Lorraine F, Kumar S (2021) Capillary-flow dynamics in open rectangular microchannels. J Fluid Mech. https://doi.org/10.1017/jfm.2020.986

Korneva G, Ye H, Gogotsi Y, Halverson D, Friedman G, Bradley J-C, Kornev KG (2005) Carbon nanotubes loaded with magnetic particles. Nano Lett 5(5):879–884

Kubochkin N, Gambaryan-Roisman T (2022) Capillary-driven flow in corner geometries. Current Opinion in Colloid Interface Science, p 101575

Lamstaes C, Eggers J (2017) Arrested bubble rise in a narrow tube. J Stat Phys 167(3):656–682

Li Z, Wang L, Li J, Chen H (2019) Drainage of lubrication film around stuck bubbles in vertical capillaries. Appl Phys Lett 115(11):111601

Manning R, Collicott S, Finn R (2011) Occlusion criteria in tubes under transverse body forces. J Fluid Mech 682:397–414

McCraney J (2023) ICF passive bubble migration meniscus locations in time. https://doi.org/10.6084/m9.figshare.22818233.v1. https://figshare.com/articles/journal_contribution/ICF_passive_bubble_migration_meniscus_locations_in_time_/22818233

McCraney J, Weislogel M, Steen P (2020) OpenFOAM simulations of late stage container draining in microgravity. Fluids 5(4):207. https://doi.org/10.3390/fluids5040207

McCraney J, Weislogel M, Steen P (2021) The draining of capillary liquids from containers with interior corners aboard the ISS. NPJ Micrograv 7(1):1–11. https://doi.org/10.1038/s41526-021-00173-5

Moher S, Weislogel M, Graf J, Soto L (2019) The dynamics of massively parallel open capillary channel systems for direct-contact liquid sorbent applications in spacecraft life support. In: 49th International Conference on Environmental Systems

Peng Y, Lin C, Li Y, Gao Y, Wang J, He J, Huang Z, Liu J, Luo X, Yang Y (2022) Identifying infectiousness of sars-cov-2 by ultra-sensitive sns2 sers biosensors with capillary effect. Matter 5(2):694–709

Stender EGP, Soumik R, Norrild RK, Aunstrup LJ, Daniel Petersen, Farzadfard A, Galvagnion C, Jensen H, Buell AK (2021) Capillary flow experiments for thermodynamic and kinetic characterization of protein liquid-liquid phase separation. Nat Commun 12(1):1–18

Torres LJ, Weislogel MM (2021) The ejection of large non-oscillating droplets from a hydrophobic wedge in microgravity. NPJ Micrograv 7(1):1–10

Weislogel MM (1996) Capillary Flow in an Interior Corner. PhD thesis, Northwestern University

Weislogel MM (2001) Capillary flow in containers of polygonal section. AIAA J 39(12):2320–2326. https://doi.org/10.2514/2.1237

Weislogel MM, Lichter S (1998) Capillary flow in an interior corner. J Fluid Mech 373:349–378. https://doi.org/10.1017/S0022112098002535

Weislogel MM, McCraney J (2019) The symmetric draining of capillary liquids from containers with interior corners. J Fluid Mech 859:902–920. https://doi.org/10.1017/jfm.2018.848

Weislogel MM, Collicott SH, Gotti Daniel J, Bunnell Charles T, Kurta Carol E, Golliher Eric L (2004) The capillary flow experiments: Handheld fluids experiments for international space station. In: AIAA Paper, pp 7408–7414, https://doi.org/10.2514/6.2004-1148

Weislogel MM, Collicott SH (2004) Capillary rewetting of vaned vontainers: spacecraft tank rewetting following thrust resettling. AIAA J 42(12):2551–2561. https://doi.org/10.2514/1.3394

Weislogel M, Jenson R, Bolleddula D (2007) *Capillary Driven Flows in Weakly 3-Dimensional Polygonal Containers*, pages 1–13. AIAA. https://doi.org/10.2514/6.2007-748

Weislogel MM, Baker JA, Jenson RM (2011) Quasi-steady capillarity-driven flows in slender containers with interior edges. J Fluid Mech 685:271–305. https://doi.org/10.1017/jfm.2011.314

Publisher's Note Springer Nature remains neutral with regard to jurisdictional claims in published maps and institutional affiliations.

Springer Nature or its licensor (e.g. a society or other partner) holds exclusive rights to this article under a publishing agreement with the author(s) or other rightsholder(s); author self-archiving of the accepted manuscript version of this article is solely governed by the terms of such publishing agreement and applicable law.

Authors and Affiliations

Joshua McCraney[1] · Joshua Bostwick[2] · Mark Weislogel[3] · Paul Steen[1]

✉ Joshua McCraney
jm2555@cornell.edu

[1] Robert Frederick Smith School of Chemical and Biomolecular Engineering, Cornell University, Ithaca, NY 14853, USA

[2] Department of Mechanical Engineering, Clemson University, Clemson, SC 29631, USA

[3] IRPI, Wilsonville, OR 97070, USA